From catastrophic collapse to multi-phase deposition: flow transformation, seafloor interaction and triggered eruption following a volcanic-island landslide

Sebastian F.L. Watt[1], Jens Karstens[2], Aaron Micallef[3], Christian Berndt[2], Morelia Urlaub[2], Melanie Ray[4], Anisha Desai[1], Maddalena Sammartini[3,6], Ingo Klaucke[2], Christoph Böttner[2], Simon Day[5], Hilary Downes[4], Michel Kühn[2], Judith Elger[2]

[1]School of Geography, Earth and Environmental Sciences, University of Birmingham, United Kingdom
[2]GEOMAR Helmholtz Centre for Ocean Research Kiel, Germany
[3]Marine Geology & Seafloor Surveying, Department of Geosciences, University of Malta, Malta
[4]Department of Earth and Planetary Sciences, Birkbeck, University of London, United Kingdom
[5]Institute for Risk and Disaster Reduction, University College London, United Kingdom
[6]Institut für Geologie, Leopold-Franzens-Universität Innsbruck, Austria

Email: s.watt@bham.ac.uk
Phone: 0044 (0)121 414 6131

Abstract

The current understanding of tsunamis generated by volcanic-island landslides is reliant on numerical models benchmarked against reconstructions of past events. As the largest historical event with timed tsunami observations, the 1888 sector collapse of Ritter Island, Papua New Guinea provides an outstanding opportunity to better understand the linked process of landslide emplacement and tsunami generation. Here, we use a combination of geophysical imaging, bathymetric mapping, seafloor observations and sampling to demonstrate that the Ritter landslide deposits are spatially and stratigraphically heterogeneous, reflecting a complex evolution of mass-flow processes. The primary landslide mass was dominated by well-bedded scoriaceous deposits, which rapidly disintegrated to form an erosive volcaniclastic flow that incised the substrate over much of its pathway. The major proportion of this initial flow is inferred to have been deposited up to 80 km from Ritter. The initial flow was followed by secondary failure of seafloor sediment, over 40 km from Ritter. The most distal part of the 1888 deposit has parallel internal boundaries, suggesting that multiple discrete units were deposited by a series of mass-flow processes initiated by the primary collapse. The last of these flows was derived from a submarine eruption triggered by the collapse. This syn-collapse eruption deposit is compositionally distinct from pre- and post-collapse eruptive products, suggesting that the collapse immediately destabilised the underlying magma reservoir. Subsequent eruptions have been fed by a modified plumbing system, constructing a submarine volcanic cone within the collapse scar through at least six post-collapse eruptions. Our results show that the initial tsunami-generating landslide at Ritter generated a stratigraphically complex set of deposits with a total volume that is several times larger than the initial failure. Given the potential for such complexity, there is no simple relationship between the volume of the tsunamigenic phase of a volcanic-island landslide and the final deposit volume, and deposit area or run-out cannot be used to infer primary landslide magnitude. The tsunamigenic potential of prehistoric sector-collapse deposits cannot, therefore, be assessed simply from surface mapping, but requires internal geophysical imaging and direct sampling to reconstruct the event.

Keywords: Sector collapse, volcanic island, tsunami, landslide, Ritter Island, Papua New Guinea

Highlights:

- Ritter Island's sector collapse provides an exemplar of volcanic tsunami hazards
- Deposit heterogeneity reflects erosion, secondary failure and a triggered eruption
- The volume of the distal deposit alone far exceeds the tsunamigenic failure
- A single catastrophic collapse led to stratigraphically complex distal deposits
- Accurate assessment of tsunami potential requires internal imaging and sampling

1. Introduction

The sector collapse of Ritter Island, Papua New Guinea (hereafter, Ritter), in 1888, reduced a conical arc-volcanic island to a crescent shaped remnant (Johnson, 1987), generating a tsunami that devastated local coastal communities and caused damage to distances of ~600 km (Day et al., 2015). The collapse is the largest historically recorded landslide at a volcanic island, and of similar scale to the Mount St. Helens sector collapse in 1980 (the headwall width of ~3 km and fall in vent elevation of ~1500 m compares with values of 2 km and 1200 m, respectively, for Mount St Helen's; cf. Glicken, 1996). The December 2018 collapse of Anak Krakatau was smaller, but emphasises the potential hazard from such events. Sector collapses occur across all volcanic settings, and their deposits have been identified around numerous arc (e.g., Deplus et al., 2001; Coombs et al., 2007; Silver et al., 2009) and intraplate (e.g., Moore et al., 1989; Masson et al., 2002, 2008) volcanic islands. Tsunami-generating volcanic-island landslides on the scale of Ritter (1-10 km^3) have global recurrence intervals of 100-200 years (Paris et al., 2014; Day et al., 2015), with all historical examples occurring in subduction-zone settings. The next large volcanic-island landslide is thus likely to be more comparable to the Ritter collapse than to the much larger events evident from deposits offshore intraplate ocean islands (e.g., the Canary Islands), which have nevertheless received more attention for their tsunamigenic potential (Ward and Day, 2001; Løvholt et al., 2008). Although contemporaneous observations from Ritter are limited due to its remote location, it is by far the largest volcanic-island landslide with timed eyewitness accounts of the generated tsunami. Of particular significance is the observation of a single tsunami wave-train, implying one phase of rapid failure and tsunami generation (Day et al., 2015).

The current understanding of landslide-generated tsunami hazards from volcanic islands is principally based on numerical models (cf. Løvholt et al., 2008; Abadie et al., 2012). Such models require an accurate representation of landslide emplacement, but this is challenging to represent due to changes in flow behaviour (for example, arising from mass disaggregation and substrate interaction). Many interpretations of volcanic-island landslide deposits are based on bathymetric observations (cf. Watt et al., 2014), providing poor volumetric constraints and a limited understanding of mass distribution and emplacement dynamics. Studies that draw on high-resolution geophysical imaging or direct sampling have shown that landslide emplacement may involve significant seafloor-sediment incorporation (Watt et al., 2012) or multi-stage deposition (Hunt et al., 2013), highlighting that accurate modelling of tsunami hazards cannot draw on a simplistic extrapolation of landslide deposit volumes.

In terms of advancing our understanding of landslide emplacement around volcanic islands, the Ritter collapse is exceptional. The deposit's relatively small dimensions and young age enable direct sampling and observations of both the scar and deposit, and spatially dense imaging by geophysical data. Here, our objective is to use new seismic-reflection, sub-bottom hydroacoustic and bathymetric data, remotely-operated vehicle (ROV) observations, and petrographic and sedimentological analyses of seafloor samples to investigate evidence of spatial and stratigraphic heterogeneity in the Ritter deposit. First, we draw on this array of data types to describe the Ritter landslide from its source to its distal deposits. We then demonstrate that compositional differences can be used to discriminate between pre- and post-collapse volcanic units, and identify evidence that the collapse triggered a submarine magmatic eruption. From these observations, we explain how a morphologically and stratigraphically complex deposit resulted from a single catastrophic collapse. Finally, we evaluate the implications of this for reconstructing volcanic-island sector collapses from their submarine depositional record, which is essential for accurate tsunami hazard modelling.

2. Previous work: 1888 landslide deposit facies

Ritter is a relatively small and morphologically youthful edifice, rising from a ~7-km wide base at ~1000 m beneath sea level. It lies between the larger islands of Umboi and Sakar at the eastern end of the Western Bismarck arc (Fig. 1), which is associated with subduction of the remnant Solomon Sea slab in an arc-continent collision environment on the north side of New Guinea (Woodhead et al., 2010). Previous surface mapping (Johnson, 1987; Silver et al., 2009; Day et al., 2015) shows that the 1888 landslide deposits can be divided into three facies based on surface morphology. The proximal facies lies within a basin bounded by the submarine flanks of Sakar and Umboi, and by two submarine volcanic ridges that formed a partial barrier and constriction to the landslide as it flowed to the west. This facies has a relatively flat surface in the north and an irregular, mounded morphology in its southern part (Fig. 1). The mounds were interpreted by Day et al. (2015) as hummocks of the type characteristic of many subaerial volcanic debris avalanches (Siebert, 1984).

Beyond the volcanic ridges, the Ritter landslide entered a deeper basin across a relatively steep slope marked by sparse mounds, W of Sakar, that was interpreted by Day et al. (2015) as the surface of a matrix-rich debris avalanche deposit (medial facies; Fig. 1). On its downslope side, the medial facies is bounded by irregular scarps that cut into well-bedded seafloor sediment. These were interpreted by Day et al. (2015) as marking sites of extensive failure of the underlying seafloor sediment. Eroded grooves in this region continue more distally (Fig. 1) across a smooth-surfaced facies, underlain by an acoustically transparent unit of relatively even thickness (termed the debris-flow facies by Day et al., 2015). Tow-camera observations and a dredge sample of cohesive intraclasts in a mud matrix (the only submarine sample previously collected from any of the Ritter deposits; Day et al., 2015) suggested that this unit comprised remobilised seafloor sediment, derived from the upslope sediment-failure scarps.

3. Methods

A research expedition on the *RV Sonne* (SO-252; November-December 2016) collected a range of data and observations around Ritter. This included a 3D seismic dataset (Karstens et al., 2019) spanning the proximal facies (Fig. 1), 2D multichannel seismic profiles (two GI-gun source with a 250-m long streamer), high-resolution sub-bottom echosounder profiles (Parasound P70 system), multibeam echosounder bathymetric and backscatter data (EM122 and EM710), seafloor photography and direct sampling. Full operational, geophysical data acquisition and processing details are provided in Berndt et al. (2017).

Imagery was collected on ten dives around Ritter and the proximal landslide facies, over a total distance of 14 km. Six of these dives used the OFOS high-resolution video sledge, and a further four used OFOS mounted on the HyBIS ROV. Samples were collected at 11 sites using a grab module mounted on HyBIS, capable of collecting up to 30 cm of seafloor sediment. A heavier grab with a wider opening, capable of 40 cm penetration, was used at one site (T1). Gravity coring was attempted at seven sites but failed to penetrate the seafloor, only retrieving small amounts of sediment in the core catcher. Grab samples that preserved intact stratigraphy were logged and subsampled as short cores. Analysed volcaniclastic samples were wet-sieved at half-phi intervals, and for finer samples particle size was determined by laser diffraction (Malvern Mastersizer 2000). Dried and sieved samples were picked for componentry (1 mm to 500 µm fraction); separated grains were mounted in resin and polished for textural imaging (scanning electron microscopy) and compositional analysis (electron microprobe analysis; Jeol JXA8100 Superprobe and Oxford Instruments AZtec system, Birkbeck College). The sites of all samples described in the text are shown in Fig. 1.

4. Landslide emplacement processes

4.1. The primary failure mass

Prior to its collapse in 1888, Ritter was a steep-sided, conical volcanic island, and numerous references in navigational reports (cf. Johnson, 1987) suggest a highly active volcano, characterised by small-scale strombolian eruptions. This is consistent with observations of the subaerial collapse headwall, which exposes interbedded scoria deposits and thin, possibly spatter-fed, lava flows, intersected by cross-cutting dykes (Fig. 2A).

Similar lithologies make up the submerged headwall, which is dominated by scoriaceous, bedded deposits in the upper part, with strongly brecciated hyaloclastite bodies becoming more frequent in deeper exposures (Fig. 2B). A highly porphyritic, mafic lithology makes up all the observed exposures. From these observations, we infer that the deeper parts of the edifice were constructed by submarine explosive and effusive activity, and that the upper flanks predominantly comprise scoriaceous material transported down the island flanks from a subaerial vent. The structure of Ritter is thus relatively simple and dominated by poorly consolidated coarse volcaniclastic units, bedded on a metre scale, alongside brecciated lavas and numerous dykes. Our observations imply that the landslide mass was relatively weak, likely to have rapidly disintegrated, and to have been dominated by sand- to cobble-sized clasts that reflect the primary grain-size range of the edifice.

4.2. Proximal landslide facies

Seafloor observations across the proximal facies support the interpretation of a weak, disintegrative landslide mass. At the mouth of the collapse amphitheatre, a prominent angular mound with well-developed parallel internal reflections (Fig. 3) is interpreted as an intact portion of the volcano flank (or toreva block). The toreva block's surface exposes a chaotic arrangement of metre-scale dense volcanic blocks (Fig. 2C.i). However, beyond this region the seafloor is ubiquitously smooth and draped in hemipelagic mud. Volcanic blocks up to 50 cm across protrude infrequently from the mud in the mounded part of the proximal landslide facies (Figs. 1 & 2C.ii). This provides clear evidence of deposition from the primary landslide mass, but seafloor observations do not suggest that individual mounds contain large (metre to decimetre scale) fragments of the edifice. Furthermore, seismic reflection profiles show that the proximal facies is underlain by folded and thrust-faulted packages of well-bedded sediment (Fig. 3A; Karstens et al., 2019). This implies that the mounded morphology in the proximal landslide facies does not reflect the transport of large, volcanic blocks of the type evident in many subaerial debris avalanche deposits (Siebert, 1984), but reflects the interplay of in-situ seafloor deformation with emplacement of an extensively disaggregated primary landslide mass. A model for how this process occurred and a description of sediment deformation in the proximal region is provided by Karstens et al. (2019), and is not discussed further here.

The margins of the mounds in the proximal landslide facies are defined by a network of channels that deepen towards the southwestern outflow of the basin (Fig. 1C), indicating incision into the deformed substrate. The summits of the mounds are deeper than the surface of the flatter area to the north, implying a maximum eroded volume of 1.6 km^3, estimated by projecting the flat northern surface across the mounded region. We infer that a mass flow derived from the disintegrating primary collapse (2.4 km^3 entirely evacuated from the collapse scar; Karstens et al., 2019) drove this erosion. Although some of this primary mass was deposited proximally and may have infilled a more irregular surface in the northern part of the basin, it does not form a seismically resolvable unit. We thus infer that much of the primary failure mass travelled beyond the proximal facies, implying that up to 4 km^3 of sediment – a volcaniclastic-hemipelagic mixture derived from Ritter and the eroded basin fill – exited the southwestern outflow of the basin (a volume closer to 3 km^3 is more likely, allowing for metre-scale deposition of the primary mass across ~50 km^2 of the proximal facies, and overestimation of channel erosion).

4.3. The medial facies

West of the submarine volcanic ridges (Fig. 1), the seafloor between Umboi and Sakar is marked by prominent mounds up to several hundred metres across, which seismic reflection profiles show are blocks rooted within partially buried, seismically-transparent packages (Fig. 3). These are interpreted as volcanic debris avalanche deposits derived from either Sakar or Umboi (based on the distribution of large blocks) and have very similar seismic characteristics to examples offshore other arc islands (Watt et al., 2012). They are interbedded with multiple thinner, tapering deposits. Given their localised extent and proximity to the steep flanks of Sakar and Umboi, we infer that this package of sediment is derived from small mass-wasting events on Sakar and Umboi.

The Ritter 1888 deposits cannot be traced into the medial facies in 2D seismic reflection profiles (and there is a lack of sub-bottom echosounder penetration), indicating that the deposit, if it exists, has a thickness of <6 m (the vertical resolution of the 2D seismic data). Direct observations here showed a smooth seafloor draped in hemipelagic mud, with no evidence of coarse clasts protruding at the surface. The lack of a seismically resolvable package, along with backscatter characteristics (general high backscatter, with linear streaks and scour around blocks rooted in deeper landslide deposits), suggests that the Ritter 1888 landslide was erosional through this area, potentially accelerating on the observed steeper gradients and due to flow constriction between Umboi and Sakar. This implies that most of the mass exiting the proximal region was ultimately deposited further downslope, in the debris-flow facies identified by Day et al. (2015). We thus reinterpret the matrix-rich facies of Day et al. as an area largely affected by erosion. The division into block- and matrix-rich facies identified at other volcanic debris avalanche deposits (e.g., Glicken, 1996) may not be applicable to the Ritter deposits, principally because of the weak, clastic nature of the primary failure mass.

4.4. Erosion and deposition in the debris-flow facies

Beyond the marginal flanks of Sakar and Umboi, seismic profiles show that the stratigraphy is characterised by parallel-bedded sediment that has accumulated on very low gradients in a basin extending ~60 km to the northwest (Fig. 3). A near-seafloor acoustically transparent deposit is observed in sub-bottom profiles across this region (Figs. 4 & 5). We infer that this represents the 1888 landslide based on its seafloor position and its continuity with seafloor erosional fabrics that extend downslope from the proximal Ritter facies. There is no evidence of any internal reflections or structure throughout the deposit, a characteristic typical of debris flow deposits (cf. Damuth, 1980). We thus retain the debris-flow facies terminology of Day et al. (2015) to refer to this unit specifically.

The debris-flow deposit forms a lobe approximately 15 km across and up to 16 m in thickness (Figs. 1A, 3B & 4), thickening towards the western margin of the basin (Fig. 5A) and extending slightly up the western edge. At the base of the deposit, stepped incisions cut into the seafloor by several metres (particularly in the proximal part of the deposit), across lateral distances of several kilometres (Fig. 5). This unequivocal evidence of seafloor erosion adds to the identification of seafloor failure scarps at the upslope margin of the facies by Day et al. (2015). Further downslope, the debris-flow deposit thins across a gradient that levels out towards a distinct break in slope (Fig. 1B). This break in slope lies above the buried distal margin of a large landslide deposit (inferred from its distribution to be from Umboi or Sakar; Fig. 3), and beyond this point the deposit forms a second lobe, of similar dimensions to that further upslope.

The two lobes of the debris flow deposit have a complex surface morphology, suggestive of spreading and subsequent erosion (Figs. 1A and 1B). The flat surface of the proximal lobe is marked by irregular furrows, which result in an angular, slab-like morphology. These are not slabs or blocks in a strict sense, since there is no evidence of internal boundaries (Fig. 5) or compositional variation within the deposit (i.e. the slabs are certainly not intact fragments of stratified sediment). The position of the furrows also shows no correlation with erosional steps at the base of the deposit, suggesting that the surficial and basal morphologies of the debris-flow facies are unrelated. The morphology may reflect across-flow velocity differences or extension affecting the deposit as it came to rest (cf. comparable morphologies in delta front debris-flow deposits; Prior et al., 1984).

The surface of the debris-flow deposit is overprinted by an erosional fabric, comprising sub-parallel grooves that extend northeast (Fig. 1A) and curve to follow the topography along the eastern margin of the basin. The direction of this fabric is slightly oblique to the maximum slope and may reflect erosion by a turbidity current deflected by topography north of Umboi (Fig. 1A). Erosional features are also evident on the surface of the distal debris-flow lobe, in the form of meandering channels and marginal incision (Fig. 1B). This erosion is inferred to represent the final phase of movement associated with the 1888 deposits.

Seafloor observations in this region indicate a smooth, featureless muddy surface. Site H6, located on the proximal debris flow lobe, recovered a disturbed 12-cm thick sample. This preserves a medium-grained volcaniclastic sand (see Section 5.3), above a silt that potentially represents the top of the debris flow deposit (Fig. 6). Site H5 was sampled within an eroded part of the distal debris-flow lobe, and comprised a homogeneous fluid mud, rich in foraminifera and containing cohesive silt and fine-sand intraclasts up to several centimetres across. This sample may entirely comprise remobilised hemipelagic mud (with fine-sand interbeds), without any material derived from Ritter itself. Although it is not necessarily representative of the entire debris flow facies, it suggests that pre-existing seafloor sediment formed a substantial component of this part of the 1888 deposits.

4.5. Distal turbidite deposition

The most distal part of the 1888 deposits form a unit contiguous with the debris-flow facies in sub-bottom profiles, but distinctive in having an extremely smooth surface and a sheet-like morphology ponded within the distal basin topography (Figs. 1, 3, 4 & 5C). The unit is acoustically distinct from underlying bedded sediment in having higher amplitude but more laterally discontinuous internal reflections, and a base characterised by a continuous high amplitude reflector. The unit contains at least three internal reflections (Fig. 5C), parallel to the unit base and surface, and its base can be mapped across a single reflector around the margins of the debris flow facies, pinching out at the basin margins. Based on these morphological characteristics and its internal boundaries we interpret this unit as a stack of turbidites derived from the 1888 collapse.

The turbidite facies is up to 10 m thick in the deepest part of the basin (Fig. 4). The top few centimetres of the facies were sampled at H4 (Fig. 1), recovering a well-sorted, fine-grained volcaniclastic sand (Fig. 6). This sample is not representative of the full unit, particularly given its internal divisions. A sand sampled at H6, in the debris flow facies, correlates with H4 based on sorting and fining relationships and compositional similarities (see Section 5). Both sands have a high bioclast content (Fig. 7), indicating seafloor sediment incorporation. The presence of mud intraclasts further supports this, and corroborates our previous inference that turbidity currents formed the erosional fabric across the debris flow facies. Although it is slightly coarser, the turbidite sand at H6 is only a few centimetres thick, suggesting that deposition from this turbidity current largely bypassed the debris-flow facies. This may also be true of the earlier turbidity currents that formed the lower units of the turbidite facies, providing a potential origin for the seafloor erosion observed at the base of the proximal debris flow lobe.

5. Impacts of collapse on volcanic processes

5.1. Post-1888 volcanism at Ritter

Submarine eruptions since the 1888 collapse (cf. Saunders and Kuduon, 2009) have formed a cone in the centre of the collapse scar (Fig. 1), ~500 m high and with a summit crater 250 m in diameter and 200 m below sea level. The cone's surface is composed of loose scoriaceous gravel (Fig. 2). A sample of this gravel (H2) shows that it comprises pale and dark vesicular components (Fig. 7), with similar phenocryst assemblages. Clinopyroxene is the dominant phase (spanning the diopside-augite field), but plagioclase is also abundant (maximum An_{91}), and both orthopyroxene and olivine are present (phenocryst cores have a maximum forsterite composition of Fo_{80}).

5.1.1. Compositional differences with pre-collapse samples

The cone samples are compositionally distinct from pre-collapse Ritter rocks sampled in the proximal landslide facies. Porphyritic lava blocks from the base of the headwall (H3; Fig. 1) are dominated by coarse (up to 5mm across), equant clinopyroxene (augite, with occasional diopside cores), with variable proportions of olivine and plagioclase. Olivine phenocrysts have dominant core compositions of $Fo_{79\text{-}80}$ (Fig. 7), but highly forsteritic grains (Fo_{89}) are also present, which we interpret as xenocrysts. Plagioclase phenocrysts show both normal and reverse zoning, reaching a maximum anorthite content of An_{90}; orthopyroxene is absent. Sand and cobble sized clasts from the mounded region of the proximal facies (H9; Fig. 1) have a similar phenocryst assemblage: clinopyroxene compositions extend slightly further into the diopside compositional field; orthopyroxene is absent; and plagioclase phenocrysts span a near identical range ($An_{76\text{-}89}$, with one outlier at An_{91}). Olivine is rare, but the only analysed olivines were of the high-forsterite type (maximum Fo_{89}). Groundmass glass analyses from several different scoriaceous clasts have a dominant silica content of 54.5-56 wt% (Fig. 8). An absence of bioclasts in the sieved fraction of sample H9 (Fig. 7) suggests that this material did not extensively mix with seafloor sediment.

The H3 sample does not represent the full spectrum of pre-collapse Ritter compositions (for example, some subaerial pre-collapse rocks contain orthopyroxene; Johnson et al., 1972), but given the sparseness of our sampling, the petrographic similarities between H3 and H9 are notable. Although H9 was transported 10 km from Ritter, it is lithologically homogeneous. We interpret that both H3 and H9 represent submarine parts of the pre-1888 Ritter edifice.

5.1.2. Post-1888 deposits across the proximal facies

In the smooth-surfaced proximal facies, 7 km WNW of the modern cone, a grab sample (T1; Fig. 1) recovered 45 cm of intact stratigraphy, comprising normally-graded mid- to dark-grey volcaniclastic sand beds, with thicknesses of 1 to >15 cm (Fig. 6). At least six well-sorted unimodal sands are present, separated by up to 20 mm of cohesive mud. These sands are compositionally and texturally similar to sample H2 form the Ritter post-1888 submarine cone: all samples contain a dark aphyric basaltic component (glass SiO_2 50-52 wt%) with rounded vesicles, as well as porphyritic vesiculated components with variable glass compositions (extending up to 65 wt% SiO_2 in pale vesiculated clasts, which are present in all the T1 beds but particularly common in T1-E (Figs. 6 & 8)). Porphyritic dark-coloured clasts are also present, and commonly have a microcrystalline groundmass, resulting in highly irregular, non-spherical vesicles (Fig. 9). The paler vesicular clasts have a glassy groundmass. Despite the broad range in glass compositions and physical appearance, the phenocryst assemblage is similar across all T1 units and clast types. Clinopyroxene and plagioclase (maximum An_{92}, with rare outliers to An_{94}) dominate, with infrequent orthopyroxene and olivine (maximum Fo_{81}).

The surficial position of the T1 volcaniclastic sands and their compositional similarities to H2 suggest that they are derived from submarine explosive eruptions at the post-1888 Ritter vent. Inter-bed differences in glass and crystal compositions, and in the relative abundance of pale and dark vesiculated clasts (Fig. 7), suggest that each T1 bed represents a discrete eruption. The products of these eruptions differ from pre-collapse rocks (H3 and H9) in both the glass and mineral compositions of the mafic components (Figs. 7 & 8), and in their textural variety and the presence of an evolved component. Comparable compositions have not been recognised in any pre-collapse subaerial or submarine samples. The T1 and H2 samples are also compositionally distinct from the scoria cones west of Ritter, which contain very primitive olivines and mantle xenoliths (Tollan et al., 2017), an observation confirmed by sample H10 ($Fo_{\sim91}$; Figs. 1 & 7).

Sample H8, collected 8 km SW of Ritter (Fig. 1) is compositionally similar to the T1 sands, leading us to conclude that an exposure of well-stratified decimetre-scale sand and mud beds (Fig. 2) at this site also represents deposits from post-1888 submarine eruptions at Ritter. 30 km west of Ritter, sample H7 preserves the top 11 cm of seafloor sediment and contains nine layers of grey silt, 1-10 mm in thickness, interbedded with cohesive mud (Fig. 6). The colour, thickness, grain-size and bedding characteristics of the silts are consistent with them being the distal equivalent of the post-1888 volcaniclastic sands at T1 and H8.

The 250-m wide crater at the summit of the post-1888 cone and the loose scoriaceous debris on its flanks implies that the cone has been constructed through submarine explosive eruptions powerful enough to eject material far above the vent. We speculate that pyroclastic material falling back from the submarine eruption column fed sediment density flows that formed the deposits identified across the basin west of Ritter. These deposits form a metre-scale veneer across the proximal landslide facies, which is not resolvable at the resolution of the seismic reflection data. We thus infer that the surface morphology of the proximal facies is a primary fabric developed during emplacement of the 1888 landslide, and has not been significantly modified by subsequent volcanism.

5.2. The distal volcaniclastic turbidite

The volcaniclastic turbidite sampled at H4 and H6, in the distal Ritter deposits, has some unexpected compositional characteristics. Rather than being mixed, as might be expected from a landslide-derived turbidite, both samples contain two discrete volcaniclastic components. Slightly over half the clasts are vesicular, mafic grains, generally aphyric and with a single dominant glass composition, identical to the post-collapse basaltic grains in T1 (and distinct from pre-collapse mafic clasts; Fig. 8). Although phenocrysts are relatively infrequent in these grains, clinopyroxene and plagioclase dominate, orthopyroxene is rare, and olivine was not analysed. Phenocryst compositions overlap with analyses of the more proximal Ritter samples (Fig. 7). A second component, making up ~25% of the samples, is a white, highly vesicular pumice (Figs. 7 & 9). The pumice glass composition is rhyolitic but relatively scattered, and more evolved than the T1 pale-coloured vesicular clasts. The pumice contains abundant phenocryst amphibole (equant, unrimmed magnesiohornblende) and plagioclase (extending to An_{60}; Fig. 7), with minor apatite and Ti-magnetite. Very rare clasts of this low-density pumice, up to 2 cm across, were found in disturbed parts of the T1 grab sample (7 km WNW of Ritter), indicating that coarser grains of the hornblende-pumice are also present near Ritter.

5.2.1. Origin of the volcanic components

The narrow compositional range of the mafic component is consistent with an origin from a single eruption. A juvenile origin is also supported by its compositional similarity with post-1888 basaltic grains, and its dissimilarity with pre-collapse samples (Fig. 8). The hornblende-pumice defines a similarly discrete population. Although the pumice could have been incorporated from a seafloor deposit (and bioclasts and mud-intraclasts certainly indicate hemipelagic sediment incorporation), this would imply a significant volumetric addition from a single, near-surface deposit. This seems unlikely to have occurred without any mafic volcaniclastic incorporation, which would have produced a wider compositional range in the mafic component. Furthermore, no comparable pumice is known from local volcanoes. Hornblende is an infrequent phenocryst phase in regional magmas, and evolved magma compositions are extremely rare (Johnson et al., 1972) throughout the Western Bismarck arc, which is dominated by mafic magmas. The coarseness of the pumice clasts at site T1, as well compositional dissimilarities, means that regional caldera-forming eruptions (Long Island, Witori and Dakataua; Fig. 1) can also be discounted as sources (Machida et al., 1996; Blong et al., 2017). The only similar local rock is a hornblende-andesite that crops out near the summit of Sakar (Johnson et al., 1972). Rocks from Sakar and Umboi are otherwise very similar to the augite-rich Ritter samples, but the Sakar andesite demonstrates that more evolved and diverse magma compositions are present in nearby magmatic systems. No pumice deposits are known from Sakar itself or in any local subaerial exposures.

The samples containing the hornblende pumice only represent the uppermost turbidite sub-unit. It is very likely that the Ritter landslide also produced a far-reaching turbidity current, and we therefore suggest that the deeper turbidite sub-units contain mixed volcaniclastic sediment from the pre-collapse edifice. The absence of pre-collapse material in the uppermost turbidite, and the erosion that overprints the debris-flow facies, suggests a time gap between the collapse and the event generating the uppermost turbidite, sufficient for the resulting sediment-flows to remain separate.

5.2.2. A collapse-triggered eruption?

Given the above observations, we suggest that the hornblende pumice is a juvenile magmatic component from a compositionally bimodal submarine eruption that followed the 1888 collapse. This eruption must have been substantially larger than subsequent (post-1888) eruptions at Ritter, given that its products were transported to much greater distances. The absence of a second documented tsunami either implies that the eruption followed the collapse within minutes (with both events contributing to a single wave train), or that any tsunami generated by the eruption was too small to be identifiable on a regional scale (no observers were present on nearby islands). The eruption vent would have been ~700 m below sea level (inferred from the base of the post-1888 cone). The occurrence of a relatively deep submarine eruption is consistent with the lack of an observed explosive eruption column following the 1888 collapse. Water-rich melts can still form pumice at depths exceeding 1000 metres (e.g., Rotella et al., 2015), and it is possible that pumice reported to have washed up on nearby beaches was derived from the eruption (Anonymous, 1888; Steinhauser, 1892). A submarine eruption, following rather than accompanying the collapse, is also consistent with the distribution of eruptive products only to the west of Ritter (sample 2A-CC, on the east flank of Ritter (Fig. 1), contains no pale vesiculated or pumiceous clasts).

Although it is possible that magma ascent preceded Ritter's sector collapse and destabilised the edifice, we suggest that the collapse itself may have triggered magma ascent due to decompression of the underlying magma reservoir. There are other examples of compositionally anomalous eruptions occurring after major sector collapses (Watt, revised), and the multiple compositional modes of younger post-collapse eruptions at Ritter (Figs. 8 & 9) point to ongoing tapping of a complex plumbing system, erupting more evolved melts than are apparent in pre-collapse rocks.

6. Summary of emplacement processes

6.1. Flow transformation and multi-phase deposition – a conceptual model

The Ritter 1888 landslide began with a single stage of tsunamigenic collapse, but the erosional patterns, morphological and compositional heterogeneities of the resultant deposits can only be explained through multiple styles and phases of mass movement. This complexity resulted from flow transformation, seafloor interaction and eruptive activity. Aspects of this process remain ambiguous, but its principal features can be constrained (Fig. 10). The initial landslide mass was highly disintegrative, and while a proportion of this material remains within the proximal region, the remaining fraction travelled through the constriction between Umboi and Sakar. In the medial facies, further downslope, there is no strong evidence of a Ritter deposit (Figs. 1 & 3). We infer that the initial volcaniclastic density current was erosive through this region. Further downslope, the leading part of this flow must have remained erosional despite a much reduced gradient, as indicated by widespread seafloor erosion (Fig. 5). We thus infer that much of the primary volcaniclastic mass that exited the proximal region was deposited in the most distal part of the Ritter deposits.

The substrate eroded by the initial flow is buried by a homogeneous debris-flow facies. An absence of internal structure within this unit suggests an extensively disaggregated mass, whose emplacement must have followed the initial erosive event. The deposit thickness and lobate forms suggest a relatively strong debris flow (cf. Talling, 2013), but the deposit does not extend upslope towards the proximal landslide facies. Our sampling of the distal debris flow lobe suggests that the major constituent of the debris-flow deposit is relatively local hemipelagic sediment. Failure of this material may have followed erosion by the initial volcaniclastic flow, retrogressively forming the scarps that mark the upslope margin of the debris flow facies (Day et al., 2015). This process may have been enhanced through deposition and loading by later volcaniclastic material exiting the proximal region. Our sampling doesn't allow us to test this, but the lack of internal boundaries within any parts of the debris-flow facies suggest its emplacement essentially involved a single phase of failure and deposition. Finally, the surface erosional fabric across the distal deposits is most easily explained by a late stage turbidity current derived from a submarine explosive eruption at Ritter, forming the compositionally-distinctive uppermost turbidite sub-unit.

The above explanation implies heterogeneity in both the type and distribution of material across the Ritter deposits. A substantial fraction of the primary failure mass was likely transported over 80 km, but deposition of this material bypassed much of the flow pathway. Conversely, much of the sediment in the debris-flow facies may have only travelled a few kilometres and be locally derived.

The different phases of movement that formed the Ritter deposits were not necessarily separated by time gaps (with the possible exception of the final eruption-generated turbidity current), but can be explained by a combination of flow transformation and secondary sediment failure. As well as forming a major component of the proximal mass affected by the landslide (Fig. 3), pre-existing sediment makes up much of the distal deposit, and the general prevalence of seafloor sediment interaction across the Ritter deposits replicates observations around other volcanic islands (Watt et al., 2012). The relative proportions of volcaniclastic and hemipelagic sediment in the distal deposit cannot be constrained, but it has a total volume of 5.0 km^3 (Fig. 4). This exceeds the volume of material exiting the proximal region (3–4 km^3, which itself includes up to 1.6 km^3 of eroded seafloor sediment), and is also a minimum estimate, since it excludes any deposition closer to Umboi and Sakar, as well as turbidite deposits outside the mapped region. The additional volume must primarily comprise seafloor sediment eroded further downstream, although a further, unconstrained component is that of the eruption-generated turbidity current.

6.2. Implications for interpreting volcanic-island landslide deposits

In a broad sense, the 1888 Ritter deposits comprise all material deformed or transported as a consequence of the volcano's sector collapse, with a total volume of ~15 km^3. However, this includes material in the proximal facies that was affected by in-situ deformation, and distal deposits from secondary sediment failure and a post-collapse eruption. Referring to this entire volume as a landslide deposit is thus somewhat misleading without an understanding of its structural and compositional heterogeneities. For landslides involving such complex emplacement processes, there is no simple relationship between deposit area and primary landslide magnitude. The processes identified here may be additional factors influencing the apparently high mobility (i.e. total downslope extent of associated deposits) of many landslides around volcanic islands (cf. Hürlimann et al., 2000). Similar emplacement complexities may be important in other submarine settings, but evidence of secondary downslope failures may be much harder to identify when the primary landslide mass is not compositionally distinctive from surrounding seafloor sediment (Gee et al., 1999).

An understanding of how the Ritter landslide was emplaced has only been achieved through internal geophysical imaging in combination with sampling, and it is reasonable to extend this conclusion to landslide deposits around other volcanic islands, where morphological complexities are often apparent (Deplus et al., 2001; Coombs et al., 2007; Watt et al., 2014). If landslide scars are obscured by subsequent volcanism, both geophysical data and sampling are likely to be required for accurate estimates of primary failure volumes, which is the critical parameter for modelling associated tsunamis.

Internal reflections show that the Ritter turbidite comprises multiple sub-units. The uppermost unit is composed of juvenile material from a post-collapse eruption, and we infer that deeper sub-units are derived from the primary failure mass. Divisions within these deeper units may reflect both compositionally discrete phases (e.g., secondary seafloor failure) and complexities introduced by transport pathways and seafloor topography (e.g., current reflection). Multi-part turbidites in several landslide-derived deposits around the Canary Islands have been inferred to represent multi-stage landslide failure (Hunt et al., 2013), implying a reduced tsunami-generating capacity. In the case of Ritter, a multi-part turbidite appears to have been generated from a single initial collapse. However, we caution against a simplistic interpretation that all landslides on volcanic islands proceed in a similar fashion. Historical sector collapses at subaerial arc volcanoes have involved a single rapid phase of movement (e.g., Mount St. Helens; Glicken, 1996), and it is unsurprising that collapses on their island equivalents are similar. This may be typical of landslides at arc volcanic islands, which have moderate dimensions (1–10 km^3) and represent the majority of tsunamigenic volcanic landslides. Major landslides in ocean-island settings are much larger (potentially far exceeding 100 km^3), but these islands are also structurally and morphologically very different to island-arc volcanoes, and their landslides may also be more shallowly seated (cf. Watt et al., 2014). It should not, therefore, be assumed that the typical style of collapse is identical across arc and ocean-island settings.

7. Conclusions

Our sedimentological and petrological analysis of seafloor samples, combined with interpretation of geophysical data and seafloor imagery, has allowed us to reconstruct the emplacement of deposits generated by the sector collapse of Ritter Island in 1888. Our results show that the primary landslide mass disintegrated rapidly and is principally distributed within a proximal basin and in the distal turbidite. Parts of the intervening region contain debris-flow deposits comprising a major proportion of disaggregated hemipelagic sediment, the failure of which appears to have been triggered following erosion by the initial volcaniclastic flow. The initial landslide was also shortly followed by a magmatic eruption, erupting both basaltic magma and a distinctive, evolved pumiceous component. The eruption of this pumice implies that more varied magma compositions exist beneath Ritter than is apparent from the stable, basaltic-andesitic pre-collapse magmatism. This is supported by the bimodal nature of repeated eruptions that have constructed a submarine cone in the collapse scar. At least six discrete eruptions have occurred since 1888, suggesting output levels that are at least comparable to Ritter's pre-collapse activity, and indicating that Ritter remains one of the region's most active volcanoes.

The total volume involved in the Ritter 1888 sector collapse (up to 15 km^3) is several times larger than the initial failure volume. The distal deposits alone (40-85 km from Ritter) have a volume far exceeding that of the initial collapse. Lateral and stratigraphic heterogeneity in the Ritter deposits results from a combination of different flow behaviours, proximal and distal seafloor erosion, secondary failure of seafloor sediment, and a magmatic eruption triggered by the initial collapse. Such complexities have only been revealed through a combination of sampling and geophysical imaging; accurate assessments of primary collapse volumes, and thus the tsunamigenic potential of ancient volcanic landslides, must therefore be based on detailed deposit characterisation and cannot be achieved by surface mapping alone.

The observation of a single tsunami wave-train at Ritter implies that the initial landslide was the principal tsunami generating mechanism, and that the triggered submarine eruption was less significant in this context. Our results also demonstrate that a single-stage collapse can result in a highly complex set of deposits. This complexity is recorded in the Ritter turbidite facies, which has internal reflections and which we conclude is stratigraphically varied (in part due to the triggered eruption). This has implications for how primary sector-collapse complexities are inferred from distal turbidite stratigraphies, although we note that sector-collapse processes should not be assumed to follow similar mechanisms across both arc and intraplate settings, given significant differences in magnitude and island structure.

Acknowledgements

We dedicate this research to the memory of co-author Melanie Ray, who made significant contributions to this research and to a much wider body of work on Ritter Island. As a valued member of the SO-252 science team, Melanie's work was important for many of the interpretations presented here. SO-252 was funded by the German ministry of Education and Research (BMBF) through the Ritter Island project 03G0252A. We thank the master of R/V Sonne and his crew for support during data collection. SW acknowledges support by the Natural Environment Research Council (NERC) grants NE/I02044X/1 & 2. AM is funded by the European Research Council under the European Union's Horizon 2020 Programme (grant agreement n° 677898 (MARCAN)). We thank Neil Mitchell and Rui Quartau for detailed and constructive reviews of this manuscript.

References

Abadie, S., Harris, J., Grilli, S., Fabre, R., 2012. Numerical modeling of tsunami waves generated by the flank collapse of the Cumbre Vieja Volcano (La Palma, Canary Islands): tsunami source and near field effects. J. Geophys. Res. 117, C05030.

Anonymous, 1888. Die Fluthwelle vom 13. Maerz 1888. Nachrichten über Kaiser Wilhelms-Land und den Bismarck-Archipel, 4(3),147-149.

Berndt, C., Muff, S., Klaucke, I., Watt, S., Böttner, C., Schramm, B., Völsch, A., Bennecke, S., Elger, J., Chi, W.-C., van Haren, J., Micallef, A., Roth, T., 2017. RV SONNE 252 Cruise Report / Fahrtbericht, Yokohama: 05.11.2016 - Nouméa: 18.12.2016. SO252: RITTER ISLAND Tsunami potential of volcanic flank collapses. Kiel, Germany, 148 pp. https://doi.org/10.3289/CR_SO252

Blong, R., Fallon, S., Wood, R., McKee, C., Chen, K., Magill, C., Barter, P., 2018. Significance and timing of the mid-17th-century eruption of Long Island, Papua New Guinea. The Holocene 28, 529-544.

Coombs, M.L., White, S.M., Scholl, D.W., 2007. Massive edifice failure at Aleutian arc volcanoes. Earth Planet. Sci. Lett. 256, 403-418.

Damuth, J.E., 1980. Use of high-frequency (3.5–12 kHz) echograms in the study of near-bottom sedimentation processes in the deep-sea: a review. Mar. Geol. 38, 51-75.

Day, S., Llanes, P., Silver, E., Hoffmann, G., Ward, S., Driscoll, N., 2015. Submarine landslide deposits of the historical lateral collapse of Ritter Island, Papua New Guinea. Mar. Petrol. Geol. 67, 419-438.

Deplus, C., Le Friant, A., Boudon, G., Komorowski, J.-C., Villemant, B., Harford, C., Ségoufin, J., Cheminée, J.-L., 2001. Submarine evidence for large-scale debris avalanches in the Lesser Antilles Arc. Earth Planet. Sci. Lett. 192, 145-157.

Gee, M.J.R., Masson, D.G., Watts, A.B., Allen, P.A., 1999. The Saharan debris flow: an insight into the mechanics of long runout submarine debris flows. Sedimentology 46, 317-335.

Glicken, H., 1996. Rockslide-debris avalanche of May 18, 1980, Mount St. Helens volcano, Washington. US Geological Survey Open File Report 96-677, 98 pp.

Hunt, J., Wynn, R., Talling, P., Masson, D., 2013. Turbidite record of frequency and source of large volume (> 100 km3) Canary Island landslides in the last 1.5 Ma: Implications for landslide triggers and geohazards. Geochem. Geophys. Geosyst. 14, 2100-2123.

Hürlimann, M., Garcia-Piera, J.O., Ledesma, A., 2000. Causes and mobility of large volcanic landslides: application to Tenerife, Canary Islands. J. Volcanol. Geotherm. Res. 103, 121-134.

Johnson, R.W., Taylor, G.A.M., Davies, R.A., 1972. Geology and petrology of Quaternary volcanic islands off the north coast of New Guinea. Australian Bureau of Mineral Resources, Geology and Geophysics Record 1972/21, 179 pp.

Johnson, R., 1987. Large-scale volcanic cone collapse: the 1888 slope failure of Ritter volcano, and other examples from Papua New Guinea. Bull. Volcanol. 49, 669-679.

Karstens, J. , Berndt, C., Urlaub, M., Watt, S.F.L., Micallef, A., Ray, M., Klaucke, I., Muff, S., Klaeschen, D., Kühn, M., Roth, T., Böttner, C., Schramm, B., Elger, J., Brune, S., 2019. From gradual spreading to catastrophic collapse – reconstruction of the 1888 Ritter Island volcanic sector collapse from high-resolution 3D seismic data. Earth Planet. Sci. Lett., accepted.

Løvholt, F., Pedersen, G., Gisler, G., 2008. Oceanic propagation of a potential tsunami from the La Palma Island. J. Geophys. Res. 113, C09026.

Machida, H., Blong, R., Specht, J., Moriwaki, H., Torrence, R., Hayakawa, Y., Talai, B., Lolok, D., Pain, C., 1996. Holocene explosive eruptions of Witori and Dakataua caldera volcanoes in west New Britain, Papua New Guinea. Quatern. Int. 34, 65-78.

Masson, D., Watts, A., Gee, M., Urgeles, R., Mitchell, N., Le Bas, T., Canals, M., 2002. Slope failures on the flanks of the western Canary Islands. Earth-Sci. Rev. 57, 1-35.

Masson, D.G., Le Bas, T.P., Grevemeyer, I, Weinrebe, W., 2008. Flank collapse and large-scale landsliding in the Cape Verde Islands, off West Africa. Geochem. Geophys. Geosyst. 9, Q07015.

Moore, J.G., Clague, D., Holcomb, R., Lipman, P., Normark, W., Torresan, M., 1989. Prodigious submarine landslides on the Hawaiian Ridge. J. Geophys. Res. 94, 17465-17484.

Paris, R., Switzer, A.D., Belousova, M., Belousov, A., Ontowirjo, B., Whelley, P.L., Ulvrova, M., 2014. Volcanic tsunami: a review of source mechanisms, past events and hazards in Southeast Asia (Indonesia, Philippines, Papua New Guinea). Nat. Hazards 70, 447-470.

Prior, D.B., Bornhold, B., Johns, M., 1984. Depositional characteristics of a submarine debris flow. J. Geol. 92, 707-727.

Rotella, M.D., Wilson, C.J., Barker, S.J., Schipper, C.I., Wright, I.C., Wysoczanski, R.J., 2015. Dynamics of deep submarine silicic explosive eruptions in the Kermadec arc, as reflected in pumice vesicularity textures. J. Volcanol. Geotherm. Res. 301, 314-332.

Saunders, S., Kuduon, J., 2009. The June 2009 Investigation of Ritter Volcano, with a Brief Discussion on its Current Nature. Papua New Guinea Department of Mineral Policy and Geohazards Management, Open File Report 003/2009, 30 pp.

Siebert, L., 1984. Large volcanic debris avalanches: characteristics of source areas, deposits, and associated eruptions. J. Volcanol. Geotherm. Res. 22, 163-197.

Silver, E., Day, S., Ward, S., Hoffmann, G., Llanes, P., Driscoll, N., Appelgate, B., Saunders, S., 2009. Volcano collapse and tsunami generation in the Bismarck volcanic arc, Papua New Guinea. J. Volcanol. Geotherm. Res. 186, 210-222.

Steinhäuser, R., 1892. Die Flutwelle und die Hilfsexpedition von Finschhafen nach der Südwestküste von Neu-Pommern. Westermanns Illustrierte deutsche Monatshefte, 71, pp. 265–75.

Talling, P.J., 2013. Hybrid submarine flows comprising turbidity current and cohesive debris flow: Deposits, theoretical and experimental analyses, and generalized models. Geosphere 9, 460-488.

Tollan, P.M.E., Dale, C., Hermann, J., Davidson, J., Arculus, R., 2017. Generation and Modification of the Mantle Wedge and Lithosphere beneath the West Bismarck Island Arc: Melting, Metasomatism and Thermal History of Peridotite Xenoliths from Ritter Island. J. Petrol. 58, 1475-1510.

Ward, S.N., Day, S., 2001. Cumbre Vieja volcano – potential collapse and tsunami at La Palma, Canary Islands. Geophys. Res. Lett. 28, 3397-3400.

Watt, S.F.L., Talling, P.J., Vardy, M.E., Masson, D.G., Henstock, T.J., Hühnerbach, V., Minshull, T.E., Urlaub, M., Lebas, E., Le Friant, A., Berndt, C., Crutchley, G.J., Karstens, J., 2012. Widespread and progressive seafloor-sediment failure following volcanic debris avalanche emplacement: Landslide dynamics and timing offshore

Montserrat, Lesser Antilles. Mar. Geol. 323, 69-94.
Watt, S.F.L., Talling, P.J., Hunt, J.E., 2014. New insights into the emplacement dynamics of volcanic island landslides. Oceanography 27, 46-57.
Watt, S.F.L., in press. The evolution of volcanic systems following sector collapse. J. Volcanol. Geotherm. Res.
Woodhead, J., Hergt, J., Sandiford, M., Johnson, W., 2010. The big crunch: physical and chemical expressions of arc/continent collision in the Western Bismarck arc. J. Volcanol. Geotherm. Res. 190, 11-24.

Figure captions

Figure 1

Bathymetric map of the seafloor around Ritter Island, Papua New Guinea, showing major morphological features of the 1888 landslide deposits (SO-252 bathymetry merged with GEBCO bathymetry outside the survey area and SRTM elevation data on land). **A** and **B** show bathymetry of two areas of the distal deposit, highlighting erosional and depositional features. The shaded relief map in **C** is coloured according to our interpreted morphological characteristics of the landslide scar and proximal facies, distinguishing pre-existing volcanic topography and the post-1888 submarine cone. Sample sites are shown in bold and image localities (Fig. 2) in italics. **D** shows a regional location map of the Bismarck arc (cf. Johnson et al., 1972; Woodhead et al., 2010).

Figure 2

Photographs of the Ritter landslide headwall, deposits and post-collapse units (locations in Fig. 1). **A**: The central portion of the subaerial headwall, showing interbedded scoriaceous deposits and parallel-bedded thin lavas dissected by cross-cutting dykes. Insets show finer-scale detail (photograph: T. Bierstedt). **B**: The submerged headwall, comprising small submarine lava bodies with poorly-developed pillow structures (B.i) or forming dense hyaloclastite breccias with alteration rinds (B.ii; arrows), interbedded with reworked volcaniclastic deposits (B.iii). **C**: The proximal facies seafloor: Dense lava blocks with planar fractured surfaces on the surface of the Toreva block at the mouth of the collapse scar (C.i); infrequent exposures of angular gravel- to cobble-sized lava clasts (rarely up to 50 cm across) protruding on the steep margins of a mound, draped by yellow hemipelagic mud (C.ii). **D**: Post-1888 deposits: loose scoriaceous gravel on the surface of the post-1888 submarine cone (D.i); volcaniclastic sands interbedded with cohesive hemipelagic mud, exposed near site H8 in the walls of shallow, rounded depressions (D.ii).

Figure 3

2D seismic reflection profile along the 1888 deposits (line position in Fig. 1), with annotated interpretations. The profile highlights the relationship between topographic changes and the deposit facies. **A** shows typical structures in the proximal landslide facies. The bold dotted line shows the base of the proximal deposits defined by Karstens et al. (2019); **B** shows details of the distal deposits and underlying stratigraphy. Selected reflectors have been picked as black lines to highlight deposit structures.

Figure 4

Thickness map of the distal 1888 Ritter deposits based on interpolated sub-bottom echosounder profiles (bathymetry contours at 50 m intervals). The mapped region has a volume of 4.97 km^3 (based on a sediment velocity of 1600 m/s) and extends as far as the unit can be imaged with high-frequency hydroacoustic data. The deposit shows two distinct acoustically-transparent lobes (interpreted as debris-flow deposits), beyond which lies a flat surfaced deposit of very regular thickness.

Figure 5

Sub-bottom echosounder profiles through the distal 1888 Ritter deposits (line positions in Fig. 4). **A** and **B** show erosional features and changes in internal and morphological characteristics across the debris flow facies (note the vertical exaggeration). **C** highlights internal reflections within the distal, flat-surfaced deposit, interpreted as a multi-unit turbidite ponded in the distal basin.

Figure 6

Logs of grab samples preserving shallow intact sections of seafloor stratigraphy (locations in Fig. 1). The volcaniclastic sands at H6 and H4 are the uppermost part of the syn-collapse turbidite. Both contain mud intraclasts and are very well sorted. Volcaniclastic sands and silts at T1 and H7 result from post-1888 eruptions at the submarine cone, and are relatively finer and thinner. The beds are unimodal and normally-graded, and interbedded with cohesive mud. The photograph shows an example of the stratigraphy. Grain-size measurements are from wet-sieving at half-phi intervals or laser-diffraction measurements (H7).

Figure 7

Sediment components and phenocryst compositions of submarine volcaniclastic samples (locations in Fig. 1). H-10C, from an outlying scoria cone, contrasts with all other samples, which are interpreted as being from Ritter. **A**: Componentry based on grain-counting of sieved 500 µm to 1 mm grain-size fractions. H4-B and H6-G (from the uppermost syn-collapse turbidite) are notable for their bioclast content. All post-collapse samples contain variable proportions of pale vesicular clasts. **B**: Plagioclase phenocryst core compositions from picked crystals or vesicular clasts. Individual analyses are shown as crosses; the grey bars mark the 5th to 95th percentile range (black line: median) for each sample group; post-collapse phenocrysts extend to higher anorthite values. A pumiceous component in the syn-collapse turbidite contains much less anorthitic phenocrysts (similar grains occur infrequently in post-collapse samples). **C**: Olivine phenocryst core compositions. Olivine is frequent in pre-collapse samples and based on two clustered populations we have interpreted a distinct, highly forsteritic xenocrystal population. This population was not found in post-collapse samples, where olivine is much less abundant but extends to slightly more forsteritic compositions than the pre-collapse phenocrysts.

Figure 8

Matrix glass compositions in vesicular grains separated from volcaniclastic samples (locations in Fig. 1). H9-B, representing pre-collapse material, spans a narrow range of basaltic andesite glass compositions. Material in the uppermost syn-collapse turbidite is distinctive from this: mafic clasts are dominated by basaltic glass, while pumiceous porphyritic clasts have a rhyolitic matrix. Post-1888 (T1) deposits are multimodal, with an aphyric basaltic component and porphyritic basaltic-andesitic to dacitic components.

Figure 9

Examples of volcanic clast textures from volcaniclastic samples. All samples contain mafic vesicular components; aphyric, glassy clasts have rounded vesicles and are basaltic in the uppermost syn-collapse turbidite and post-collapse deposits, but basaltic-andesite in the proximal landslide sample (H9-B). Porphyritic mafic clasts are common in T1 samples and typically have microcrystalline groundmasses, resulting in very irregular vesicles (T1-C image), but in some cases are glassy, with a basaltic-andesite composition (T1-I image). Pale vesicular clasts are also frequent in T1 samples and have more evolved glass compositions. All clast types contain highly anorthitic and overlapping plagioclase populations ($An_{x\%}$ values). In contrast, the pale vesicular clasts in the syn-collapse turbidite (H6-G image) contain less anorthitic phenocrysts and hornblende, and have a very open, pumiceous texture.

Figure 10
A summary of processes involved in the emplacement of the 1888 Ritter landslide deposits. The topographic profile shows a transect along the flow pathway (approximately equivalent to that shown in Fig. 3), with variable vertical exaggeration.

Supplementary Data
1. Site coordinates and descriptions of all sampling sites and of images used in the text, with sample descriptions and images (.pdf).
2. Mineral compositions for data plotted in Figs. 7 and 8 and referred to in text.

Figure1

Click here to download Figure: Fig1comp.pdf

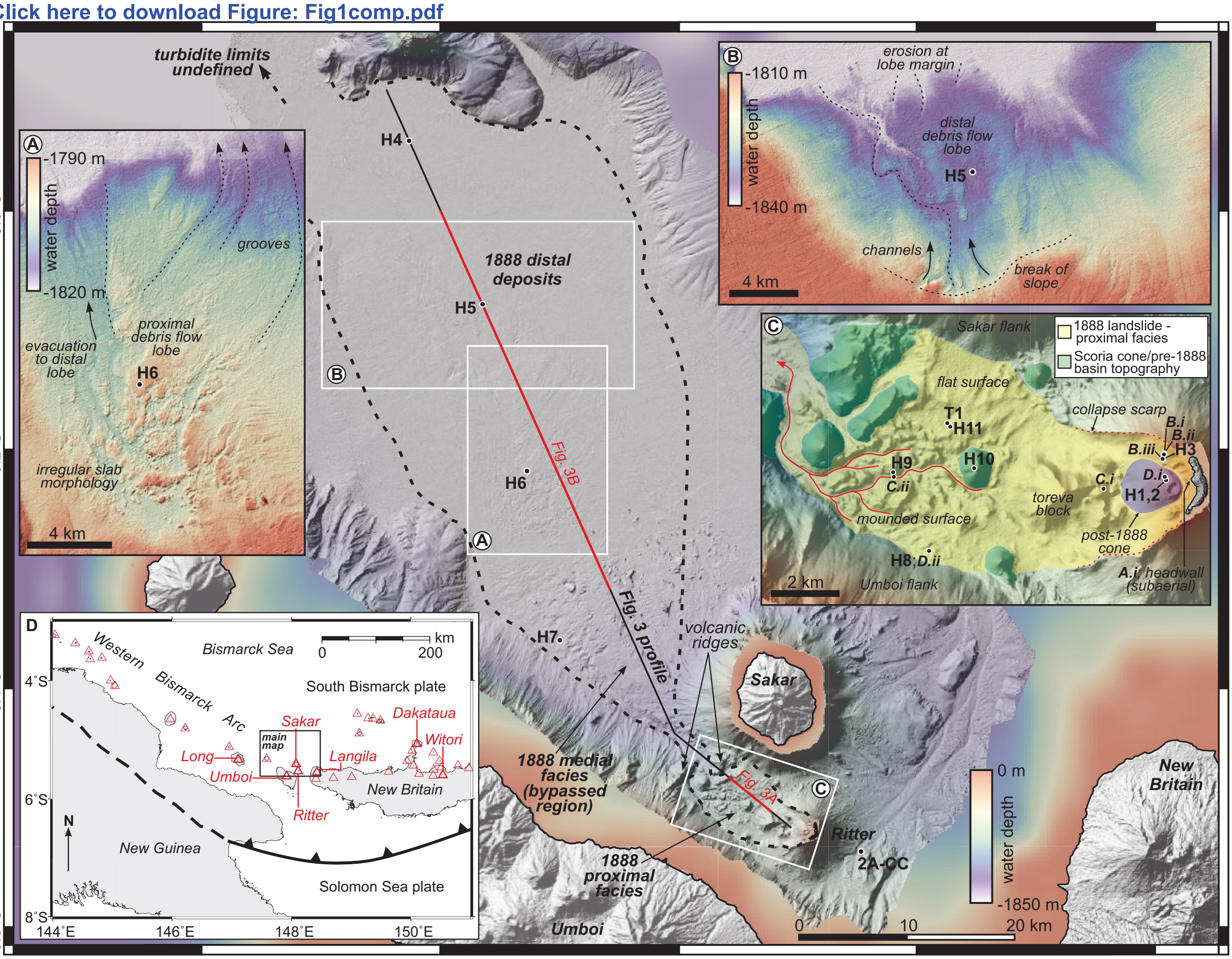

Figure2

Click here to download Figure: Fig2comp.pdf

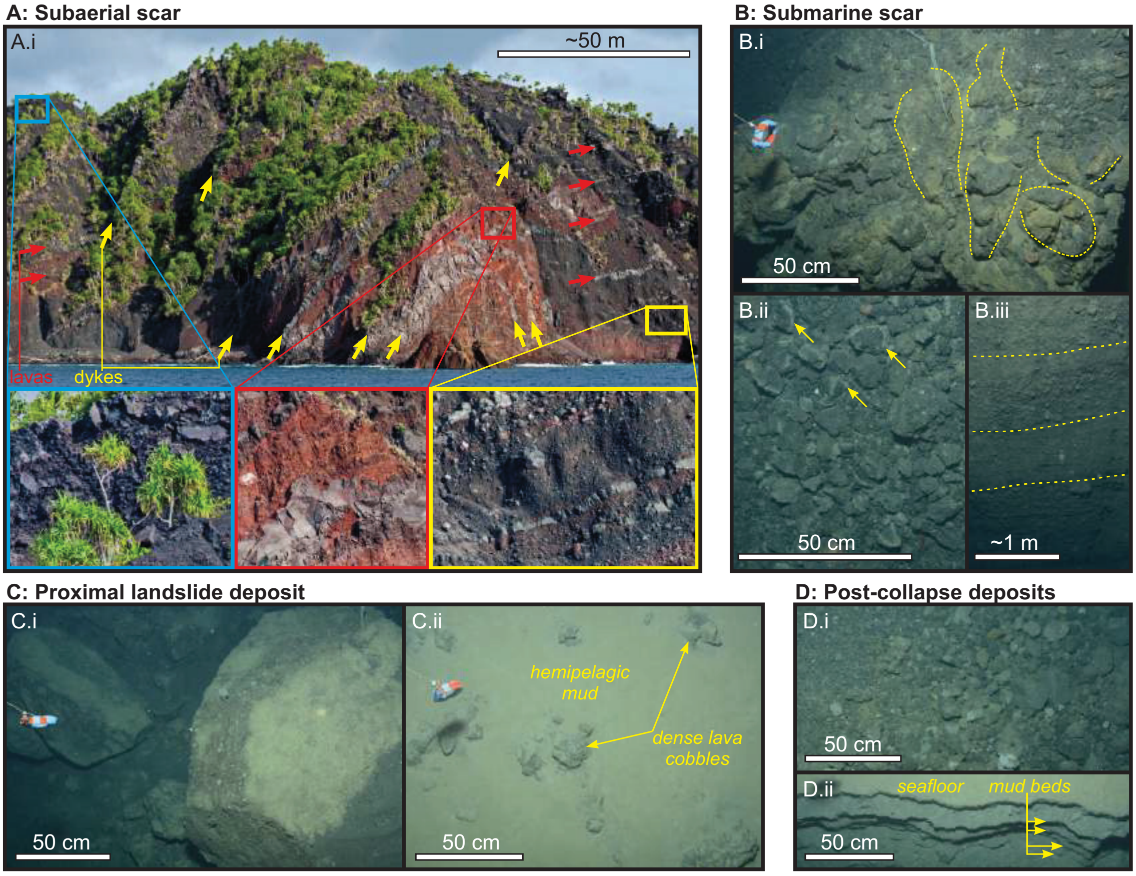

Figure3

Click here to download Figure: Fig3comp.pdf

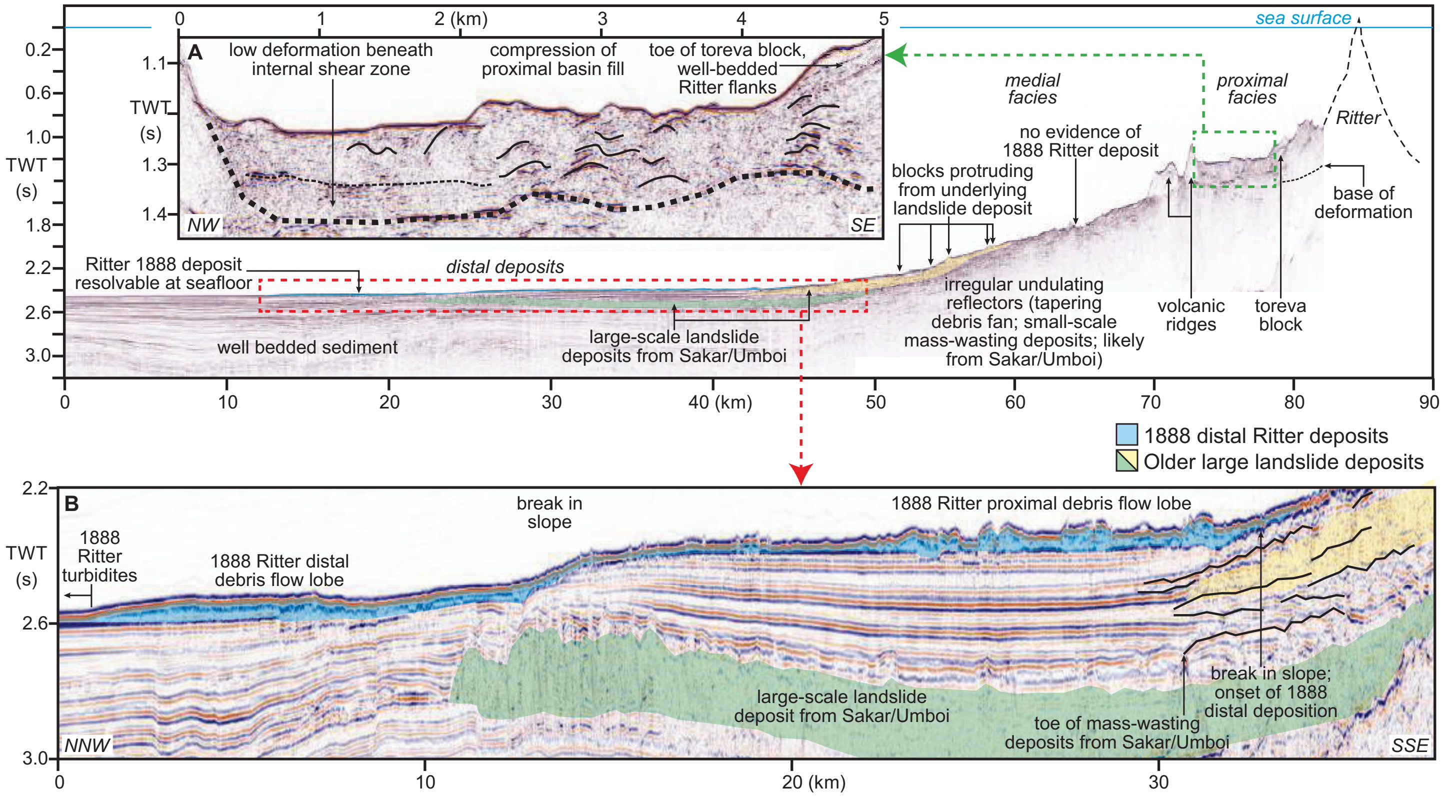

Figure4
Click here to download Figure: Fig4comp.pdf

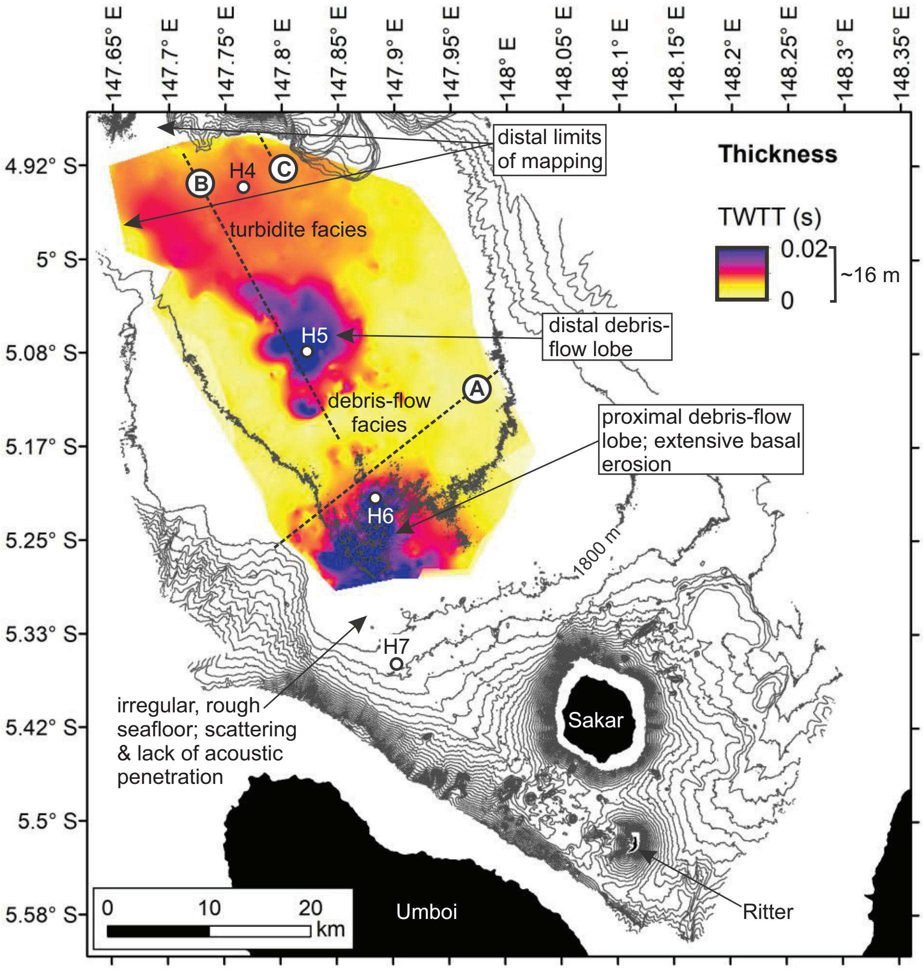

Figure5

Click here to download Figure: Fig5comp.pdf

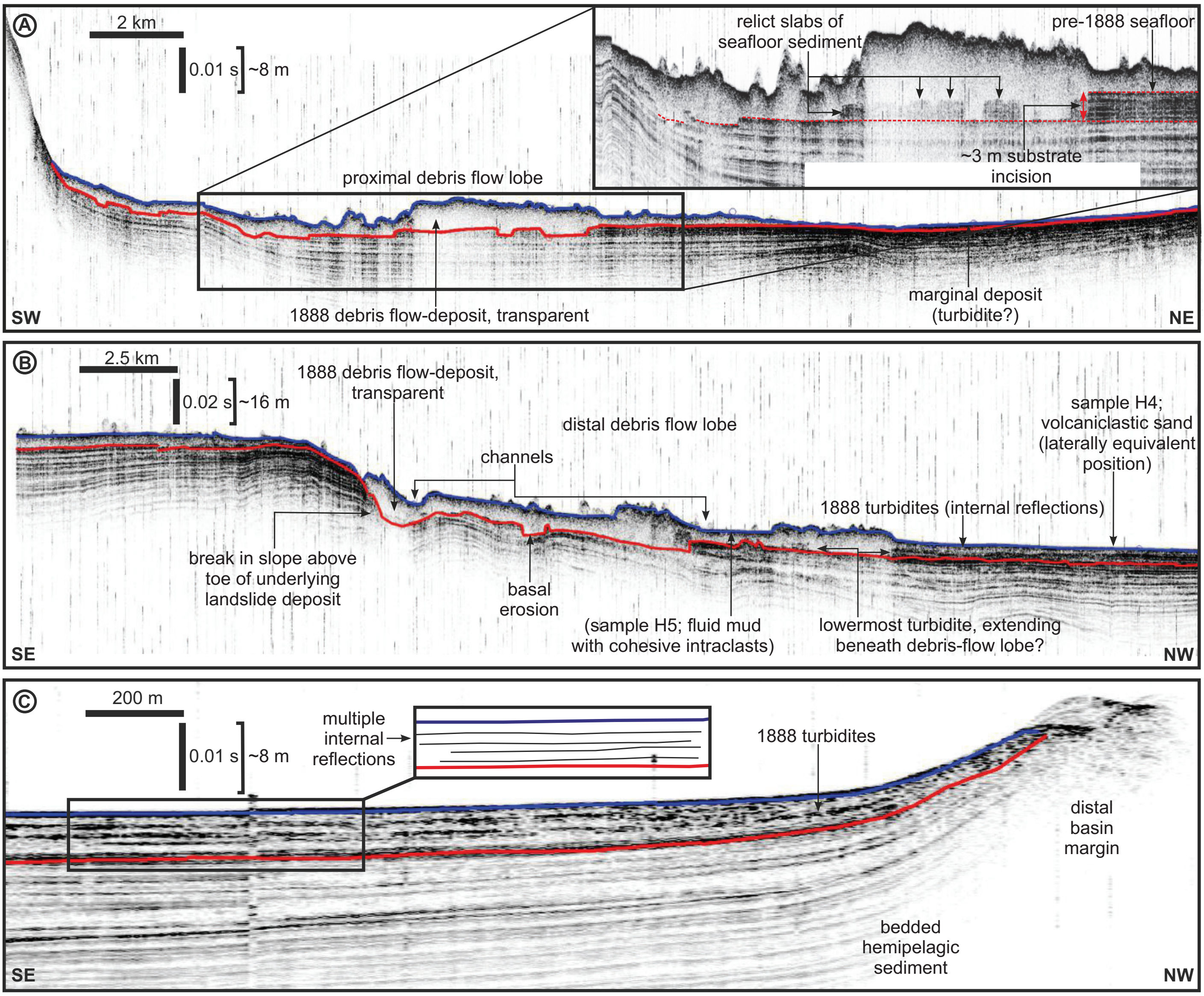

Figure6

Click here to download Figure: Fig6comp.pdf

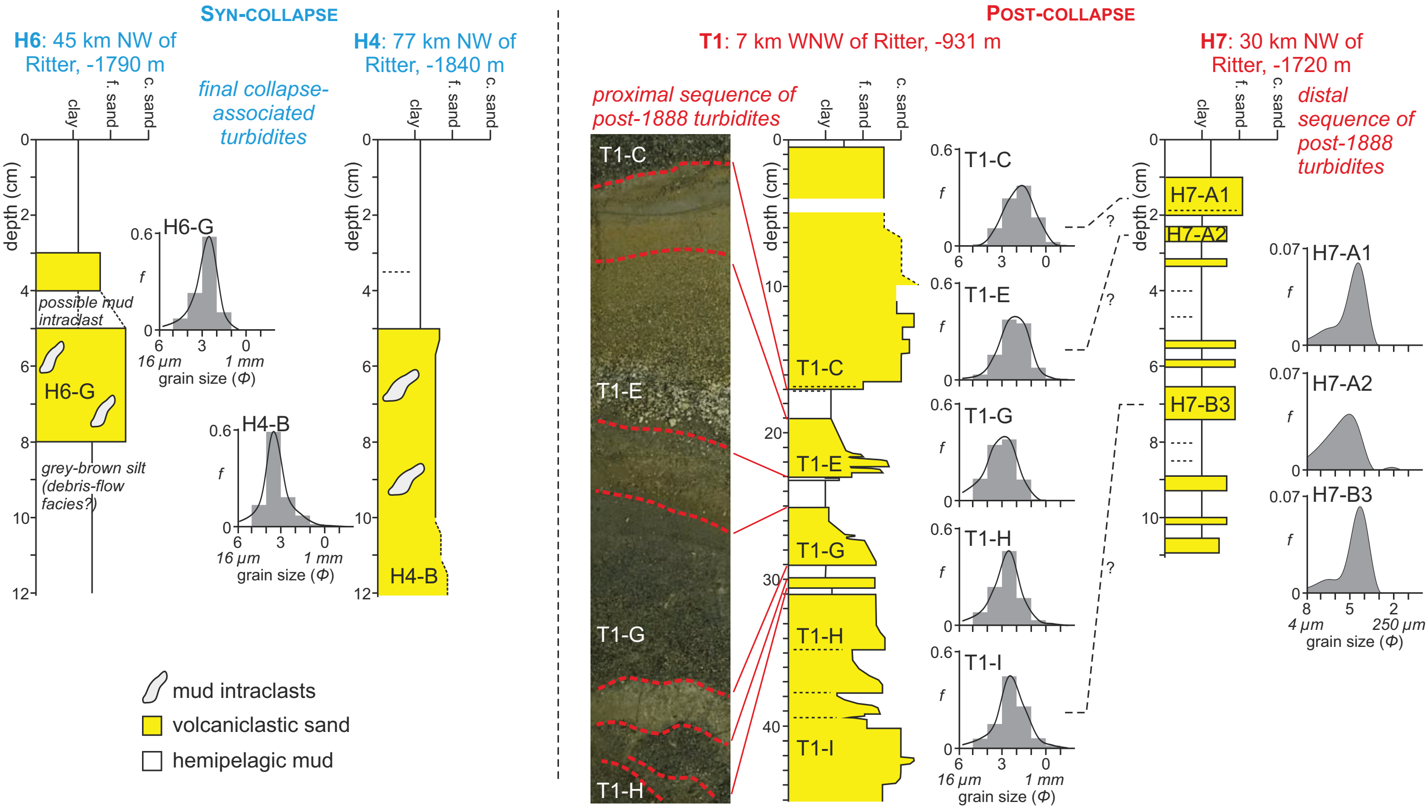

Figure7

Click here to download Figure: Fig7comp.pdf

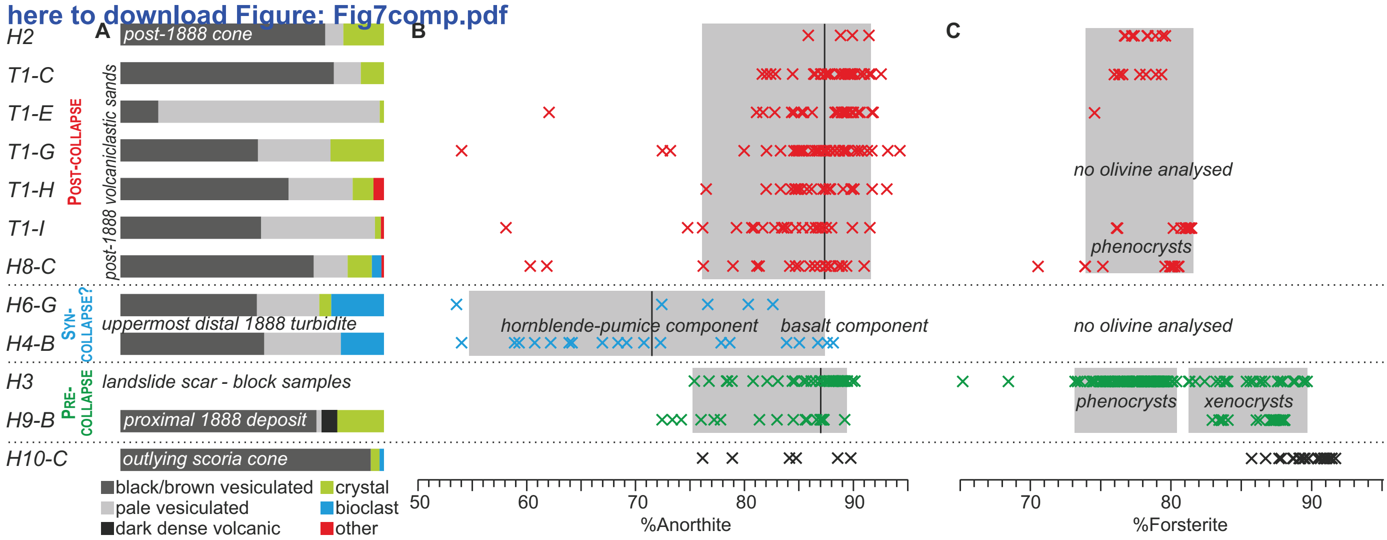

Figure8

Click here to download Figure: Fig8comp.pdf

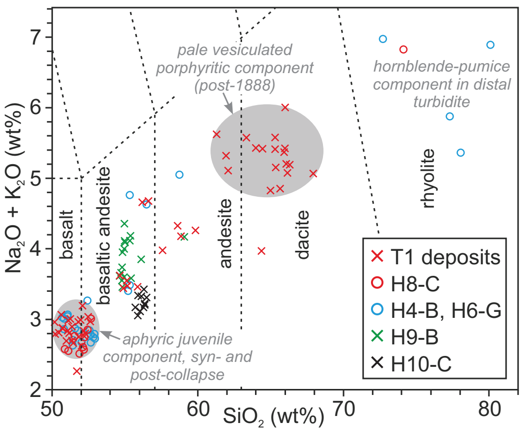

Figure9

Click here to download Figure: Fig9comp.pdf

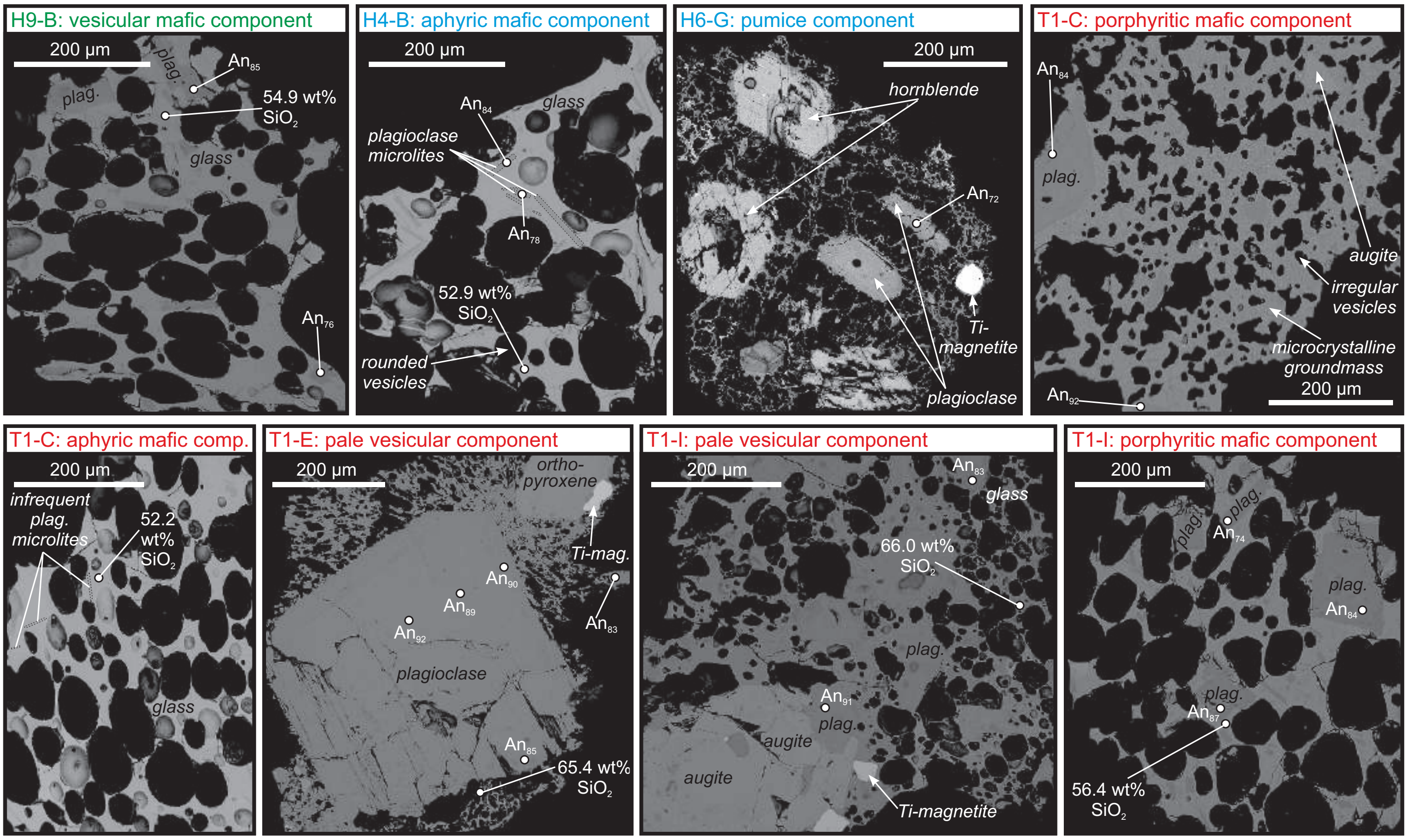

Figure10

Click here to download Figure: Fig10comp.pdf